Supplemental Information

Supplemental methods

Wildfire severity typically describes the proportion of vegetation mortality resulting from fire (1), and can be measured by comparing pre- and postfire satellite imagery for a specific area (2). This usually requires considerable manual effort for image collation and processing, followed by calibration with field data (3–11). Hurculean efforts to measure severity across broad spatial extents, such as the Monitoring Trends in Burn Severity project (12), exist but often must sacrifice coverage of smaller fires which are far more common (13), may have different severity expectations compared to larger fires (14, 15), and are generally important contributors to global fire effects (16). Automated efforts to remotely assess wildfire have arisen, but they tend to focus on more aggregate measures of wildfire such as whether an area burned or the probability that it burned rather than the severity of the burn (17–20), but see (21, 22). Here, we present a method to automate the measurement of wildfire severity using minimal user inputs: a geometry of interest (a wildfire perimeter or a field plot location) and an alarm date (the date the fire was discovered). This information is readily available in many fire-prone areas (such as California, via the Fire and Resource Assessment Program; http://frap.fire.ca.gov/projects/fire_data/fire_perimeters_index) or could be derived using existing products (such as the Landsat Burned Area Essential Climate Variable product described in (20)).

Vegetation characteristics can be measured using remotely-sensed imagery (23–25) and texture analysis of this imagery can quantify ecologically relevant local environmental heterogeneity across broad spatial extents (26–30), which may be used as a direct measure of ecosystem resilience (31). Developed for image classification and computer vision, texture analysis characterizes each pixel in an image by a summary statistic of its neighboring pixels, and represents a measure of local heterogeneity which itself varies across the landscape (32). Texture analysis of forested areas detects heterogeneity of overstory vegetation, which corresponds to fuel loading and continuity, capturing the primary influence of vegetation structure on fire behavior.

We calibrate 56 configurations of our algorithmic approach to ground-based wildfire severity measurements, and select the best performing severity metric to generate a comprehensive, system-wide severity dataset.

Normalized difference vegetation index (NDVI; Supplemental Equation 1) correlates with vegetation density, canopy cover, and leaf area index (23). Normalized difference moisture index (NDMI; Supplemental Equation 2) correlates with similar vegetation characteristics as NDVI, but doesn't saturate at high levels of foliar biomass (33). Normalized burn ratio (NBR; Supplemental Equation 3) and normalized burn ratio version 2 (NBR2; Supplemental Equation 4) respond strongly to fire effects on vegetation (2, 20, 35–37).

$$(1)\ \ ndvi = (nir - red)/(nir + red)$$

$$(2)\ \ ndmi = (nir - swir1)/(nir + swir1)$$

$$(3)\ \ nbr = (nir - swir2)/(nir + swir2)$$

$$(4)\ \ nbr2 = (swir1 - swir2)/(swir1 + swir2)$$

Where nir is the near infrared band (band 4 on Landsat 4, 5, and 7; band 5 on Landsat 8) and red is the red band (band 3 on Landsat 4, 5, and 7; band 4 on Landsat 8), $swir1$ is the first short wave infrared band (band 5 on Landsat 4, 5, and 7; band 4 on Landsat 8), $swir2$ is the second short wave infrared band (band 7 on Landsat 4, 5, 7, and 8)

We calculated the delta severity indices (dNBR, dNBR2, dNDVI) by subtracting the respective postfire indices from the prefire indices (NBR, NBR2, and NDVI) without multiplying by a rescaling constant (e.g., we did not multiply the result by 1000 as in (3); Supplemental Equation 5). Following (21), we chose not to correct the delta indices using a phenological offset value (typically calculated as the delta index in homogeneous forest patch outside of the fire perimeter), as our approach implicitly accounts for phenology by incorporating multiple cloud-free images across the same time window both before the fire and one year later.

$$(5)\ \ dI = I_{\text{prefire}} - I_{\text{postfire}}$$

We calculated the relative delta severity indices, RdNBR and RdNDVI, by scaling the respective delta indices (dNBR and dNDVI) from Supplemental Equation 6 by a square root transformation of the absolute value of the prefire index:

$$(6)\ \ RdI = \frac{dI}{\sqrt{|I_{\text{prefire}}|}}$$

We calculated the relative burn ratio (RBR) following (8) using Supplemental Equation 7:

$$(7)\ \ RBR = \frac{dNBR}{NBR_{\text{prefire}} + 1.001}$$

We used the digital elevation model to calculate the potential annual heat load (Supplemental Equation 8 at each pixel, which is an integrated measure of latitude, slope, and a folding transformation of aspect about the northeast-southwest line, such that northeast becomes 0 radians and southwest becomes π radians (38, 39):

$$aspect_{folded} = |\pi - |aspect - \frac{5\pi}{4}||$$

$$\log(pahl) = \begin{aligned} & -1.467+ \\ & 1.582 * cos(latitude)cos(slope)- \\ & 1.5 * cos(aspect_{folded})sin(slope)sin(latitude)- \\ & 0.262 * sin(lat)sin(slope)+ \\ & 0.607 * sin(aspect_{folded})sin(slope) \end{aligned} \quad (8)$$

Where *pahl* is the potential annual heat load, $aspect_{folded}$ is a transformation of aspect in radians, and both *latitude* and *slope* are extracted from a digital elevation model with units of radians.

Supplemental figures and tables

Supplemental Table 1: Comparison of models used to validate and calibrate remotely sensed wildfire severity with ground-based composite burn index (CBI) severity sorted in descending order by the R^2 value from a 5-fold cross validation. A total of 56 models were tested representing all possible combinations of 7 different measures of wildfire severity (RBR, dNBR, dNBR2, RdNBR, RdNBR2, dNDVI, and RdNDVI), 4 different time windows in which Landsat imagery was acquired and summarized with a median reducer on a pixel-by-pixel basis (16 days, 32 days, 48 days, and 64 days), and two different interpolation methods (bilinear and bicubic). The three parameters (β_0, β_1, and β_2) from the nonlinear model fit described in Eq. 1 are reported. For each model, the value of the remotely sensed wildfire severity measurement corresponding to the lower bounds of 3 commonly used categories of severity are reported ('low' corresponds to a CBI value of 0.1, 'mod' corresponds to a CBI value of 1.25, and 'high' corresponds to a CBI value of 2.25)

Rank	Severity measure	Time window	Interpolation	k-fold R^2	β_0	β_1	β_2	low	mod	high
1	RBR	48	bicubic	0.82	0.014	0.028	1.001	0.045	0.113	0.282
2	RdNBR	32	bilinear	0.813	-0.483	3.061	0.857	2.852	8.45	20.56
3	RdNDVI	48	bilinear	0.809	-2.144	3.273	0.609	1.335	4.867	10.75
4	RBR	32	bilinear	0.807	0.014	0.029	0.985	0.046	0.113	0.28
5	RdNDVI	64	bicubic	0.805	-2.524	3.57	0.59	1.263	4.936	10.93
6	RBR	64	bicubic	0.805	0.016	0.027	1.01	0.046	0.113	0.283
7	RdNDVI	32	bicubic	0.803	-2.737	3.308	0.619	0.782	4.436	10.59
8	RBR	64	bilinear	0.802	0.017	0.027	1.003	0.047	0.113	0.279
9	RdNDVI	32	bilinear	0.801	-2.531	3.176	0.624	0.849	4.393	10.39
10	RdNDVI	48	bicubic	0.797	-2.623	3.624	0.587	1.22	4.922	10.94
11	RdNDVI	64	bilinear	0.796	-2.14	3.287	0.607	1.353	4.876	10.73
12	RdNBR	64	bilinear	0.792	-0.42	3.031	0.862	2.884	8.483	20.66

Rank	Severity measure	Time window	Interpolation	k-fold R^2	β_0	β_1	β_2	low	mod	high
13	RBR	48	bilinear	0.791	0.017	0.027	1.006	0.047	0.112	0.277
14	RBR	32	bicubic	0.79	0.013	0.029	0.994	0.045	0.114	0.284
15	RdNBR	48	bicubic	0.785	-0.858	3.219	0.852	2.647	8.476	21.02
16	RBR	16	bilinear	0.781	0.021	0.026	1.016	0.05	0.114	0.278
17	RdNBR	32	bicubic	0.776	-0.954	3.34	0.841	2.679	8.602	21.2
18	dNDVI	32	bicubic	0.776	-0.058	0.073	0.65	0.02	0.106	0.257
19	dNBR	48	bicubic	0.775	0.03	0.035	1.069	0.068	0.161	0.413
20	RdNBR	16	bilinear	0.774	0.279	2.518	0.909	3.037	8.119	19.73
21	dNDVI	32	bilinear	0.772	-0.053	0.07	0.656	0.022	0.105	0.252
22	dNDVI	48	bicubic	0.772	-0.055	0.081	0.613	0.031	0.119	0.267
23	dNBR	32	bilinear	0.77	0.029	0.036	1.048	0.069	0.163	0.41
24	RdNBR2	64	bicubic	0.766	2.102	0.416	1.24	2.572	4.059	8.861
25	dNBR	32	bicubic	0.764	0.028	0.036	1.057	0.068	0.163	0.417
26	dNDVI	48	bilinear	0.762	-0.044	0.073	0.637	0.034	0.118	0.262
27	RBR	16	bicubic	0.761	0.021	0.026	1.028	0.049	0.114	0.281
28	dNBR	16	bilinear	0.76	0.033	0.036	1.048	0.073	0.167	0.417
29	RdNBR2	32	bilinear	0.759	1.435	0.625	1.1	2.132	3.906	8.861
30	RdNBR	16	bicubic	0.758	0.37	2.446	0.926	3.053	8.149	20
31	RdNBR2	32	bicubic	0.754	1.426	0.601	1.125	2.098	3.876	8.975
32	dNBR	64	bicubic	0.753	0.033	0.033	1.086	0.07	0.161	0.413
33	dNBR	64	bilinear	0.751	0.035	0.033	1.08	0.071	0.161	0.406
34	RdNBR2	48	bicubic	0.751	1.835	0.46	1.209	2.354	3.919	8.818
35	dNBR	48	bilinear	0.748	0.035	0.033	1.076	0.071	0.161	0.405
36	RdNDVI	16	bilinear	0.747	-0.983	2.503	0.678	1.695	4.856	10.52
37	dNDVI	64	bicubic	0.746	-0.055	0.082	0.609	0.032	0.12	0.266
38	dNDVI	64	bilinear	0.741	-0.046	0.075	0.627	0.034	0.118	0.261
39	RdNBR2	48	bilinear	0.737	1.802	0.497	1.174	2.361	3.956	8.766
40	RdNBR	64	bicubic	0.737	-1.448	3.651	0.819	2.515	8.717	21.61
41	RdNBR2	64	bilinear	0.735	2.027	0.451	1.204	2.536	4.06	8.801
42	dNBR	16	bicubic	0.729	0.032	0.036	1.058	0.072	0.168	0.423

Rank	Severity measure	Time window	Interpolation	k-fold R^2	β_0	β_1	β_2	low	mod	high
43	dNBR2	32	bilinear	0.727	0.026	0.009	1.149	0.035	0.062	0.14
44	dNDVI	16	bicubic	0.726	-0.03	0.065	0.674	0.04	0.121	0.267
45	RdNDVI	16	bicubic	0.725	-1.248	2.681	0.665	1.618	4.908	10.72
46	dNBR2	32	bicubic	0.715	0.025	0.008	1.177	0.035	0.061	0.142
47	dNBR2	64	bilinear	0.714	0.036	0.006	1.283	0.043	0.064	0.137
48	dNDVI	16	bilinear	0.707	-0.023	0.06	0.689	0.042	0.12	0.261
49	dNBR2	48	bilinear	0.686	0.033	0.006	1.248	0.04	0.063	0.137
50	RdNBR2	16	bilinear	0.682	1.928	0.465	1.189	2.452	3.983	8.676
51	dNBR2	16	bilinear	0.662	0.03	0.009	1.138	0.04	0.066	0.143
52	RdNBR2	16	bicubic	0.654	1.871	0.467	1.198	2.398	3.96	8.792
53	dNBR2	16	bicubic	0.635	0.029	0.009	1.156	0.039	0.066	0.145
54	RdNBR	48	bilinear	0.63	-3.445	5.132	0.724	2.072	9.235	22.7
55	dNBR2	48	bicubic	0	0.033	0.006	1.284	0.04	0.062	0.138
56	dNBR2	64	bicubic	0	0.037	0.005	1.313	0.043	0.064	0.139

Supplemental Table 2: Model parameter estimates for different neighborhood sizes. Values represent the mean parameter estimates with 95% credible intervals in parentheses.

Coefficient	90m x 90m neighborhood	150m x 150m neighborhood	210m x 210m neighborhood	270m x 270m neighborhood
β_0	-2.415 (-2.588, -2.255)	-2.432 (-2.605, -2.271)	-2.447 (-2.619, -2.279)	-2.45 (-2.618, -2.288)
$\beta_{nbhd\_stdev\_NDVI}$	-0.208 (-0.247, -0.17)	-0.212 (-0.255, -0.17)	-0.203 (-0.248, -0.158)	-0.195 (-0.242, -0.148)
$\beta_{prefire\_NDVI}$	1.044 (0.911, 1.174)	1.13 (1.028, 1.229)	1.141 (1.057, 1.222)	1.132 (1.056, 1.209)
β_{fm100}	-0.569 (-0.71, -0.423)	-0.564 (-0.709, -0.419)	-0.561 (-0.697, -0.428)	-0.565 (-0.712, -0.422)
β_{pahl}	0.239 (0.208, 0.271)	0.238 (0.205, 0.269)	0.239 (0.207, 0.269)	0.24 (0.209, 0.272)

Coefficient	90m x 90m neighborhood	150m x 150m neighborhood	210m x 210m neighborhood	270m x 270m neighborhood
$\beta_{\text{topographic\_roughness}}$	-0.01 (-0.042, 0.022)	-0.006 (-0.039, 0.027)	-0.002 (-0.037, 0.032)	-0.002 (-0.036, 0.033)
$\beta_{\text{nbhd\_mean\_NDVI}}$	-0.14 (-0.278, 0.002)	-0.265 (-0.381, -0.148)	-0.293 (-0.392, -0.193)	-0.293 (-0.389, -0.198)
$\beta_{\text{nbhd\_stdev\_NDVI*prefire\_NDVI}}$	0.125 (0.029, 0.218)	0.06 (-0.013, 0.135)	0.022 (-0.045, 0.09)	0.009 (-0.054, 0.072)
$\beta_{\text{nbhd\_stdev\_NDVI*nbhd\_mean\_NDVI}}$	-0.129 (-0.223, -0.034)	-0.078 (-0.151, -0.006)	-0.03 (-0.095, 0.035)	-0.006 (-0.068, 0.054)
$\beta_{\text{nbhd\_stdev\_NDVI*fm100}}$	-0.037 (-0.081, 0.006)	-0.035 (-0.078, 0.01)	-0.03 (-0.076, 0.014)	-0.023 (-0.07, 0.023)
$\beta_{\text{nbhd\_mean\_NDVI*prefire\_NDVI}}$	-0.573 (-0.62, -0.526)	-0.564 (-0.612, -0.516)	-0.549 (-0.596, -0.502)	-0.537 (-0.587, -0.49)

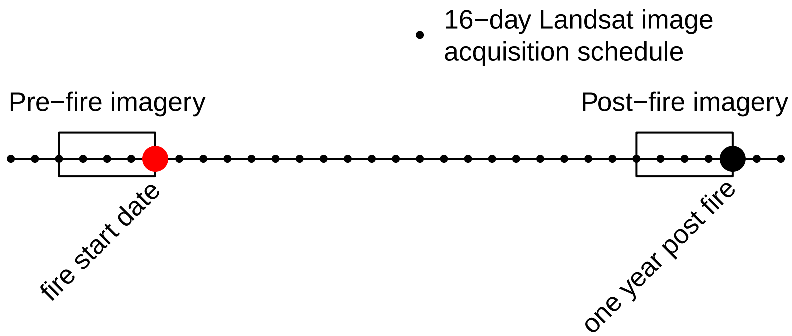

Supplemental Figure 1: Schematic for how Landsat imagery was assembled in order to make comparisons between pre- and post-fire conditions. This schematic depicts a 64-day window of image collation prior to the fire which comprise the pre-fire image collection. A similar, 64-day window collection of imagery is assembled one year after the pre-fire image collection.

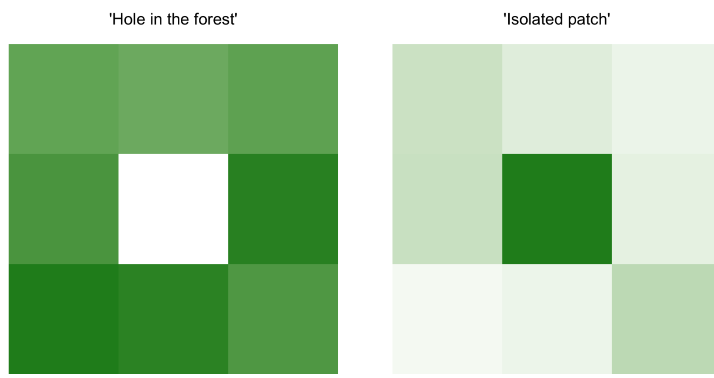

Supplemental Figure 2: Conceptual diagram of 'decoupling' that sometimes occurs between the central pixel NDVI and the neighborhood mean NDVI. In each of these scenarios, our model results suggest that the probability that the central pixel burns at high severity is higher than expected given the additive effect of the covariates. The left panel depicts the "hole in the forest" decoupling, which occurs more frequently, and the right panel depicts the "isolated patch" decoupling.

References

1. Keeley JE (2009) Fire intensity, fire severity and burn severity: A brief review and suggested usage. *International Journal of Wildland Fire* 18(1):116.

2. Key CH, Benson NC (2006) Landscape Assessment (LA). 55.

3. Miller JD, Thode AE (2007) Quantifying burn severity in a heterogeneous landscape with a relative version of the delta Normalized Burn Ratio (dNBR). *Remote Sensing of Environment* 109(1):66–80.

4. Miller JD, et al. (2009) Calibration and validation of the relative differenced Normalized Burn Ratio (RdNBR) to three measures of fire severity in the Sierra Nevada and Klamath Mountains, California, USA.

Remote Sensing of Environment 113(3):645–656.

5. De Santis A, Asner GP, Vaughan PJ, Knapp DE (2010) Mapping burn severity and burning efficiency in California using simulation models and Landsat imagery. *Remote Sensing of Environment* 114(7):1535–1545.

6. Cansler CA, McKenzie D (2012) How Robust Are Burn Severity Indices When Applied in a New Region? Evaluation of Alternate Field-Based and Remote-Sensing Methods. *Remote Sensing* 4(2):456–483.

7. Veraverbeke S, Hook SJ (2013) Evaluating spectral indices and spectral mixture analysis for assessing fire severity, combustion completeness and carbon emissions. *International Journal of Wildland Fire* 22(5):707.

8. Parks S, Dillon G, Miller C (2014) A New Metric for Quantifying Burn Severity: The Relativized Burn Ratio. *Remote Sensing* 6(3):1827–1844.

9. Prichard SJ, Kennedy MC (2014) Fuel treatments and landform modify landscape patterns of burn severity in an extreme fire event. *Ecological Applications* 24(3):571–590.

10. Edwards AC, Russell-Smith J, Maier SW (2018) A comparison and validation of satellite-derived fire severity mapping techniques in fire prone north Australian savannas: Extreme fires and tree stem mortality. *Remote Sensing of Environment* 206:287–299.

11. Fernández-García V, et al. (2018) Burn severity metrics in fire-prone pine ecosystems along a climatic gradient using Landsat imagery. *Remote Sensing of Environment* 206:205–217.

12. Eidenshink J, et al. (2007) A Project for Monitoring Trends in Burn Severity. *Fire Ecology* 3(1):3–21.

13. Calkin DE, Gebert KM, Jones JG, Neilson RP (2005) Forest Service Large Fire Area Burned and Suppression Expenditure Trends, 19702002. *j for* 103(4):179–183.

14. Cansler CA, McKenzie D (2014) Climate, fire size, and biophysical setting control fire severity and spatial pattern in the northern Cascade Range, USA. *Ecological Applications* 24(5):1037–1056.

15. Harvey BJ, Donato DC, Turner MG (2016) Drivers and trends in landscape patterns of stand-replacing fire in forests of the US Northern Rocky Mountains (1984-2010). *Landscape Ecology* 31(10):2367–2383.

16. Randerson JT, Chen Y, Werf GR van der, Rogers BM, Morton DC (2012) Global burned area and biomass burning emissions from small fires. *Journal of Geophysical Research: Biogeosciences* 117(G4). doi:10.1029/2012JG002128.

17. Bastarrika A, Chuvieco E, Martín MP (2011) Mapping burned areas from Landsat TM/ETM+ data with a two-phase algorithm: Balancing omission and commission errors. *Remote Sensing of Environment*

115(4):1003–1012.

18. Goodwin NR, Collett LJ (2014) Development of an automated method for mapping fire history captured in Landsat TM and ETM+ time series across Queensland, Australia. *Remote Sensing of Environment* 148:206–221.

19. Boschetti L, Roy DP, Justice CO, Humber ML (2015) MODISLandsat fusion for large area 30m burned area mapping. *Remote Sensing of Environment* 161:27–42.

20. Hawbaker TJ, et al. (2017) Mapping burned areas using dense time-series of Landsat data. *Remote Sensing of Environment* 198:504–522.

21. Reilly MJ, et al. (2017) Contemporary patterns of fire extent and severity in forests of the Pacific Northwest, USA (1985-2010). *Ecosphere* 8(3):e01695.

22. Parks SA, et al. (2018) High-severity fire: Evaluating its key drivers and mapping its probability across western US forests. *Environmental Research Letters* 13(4):044037.

23. Rouse W, Haas RH, Deering W, Schell JA (1973) *MONITORING THE VERNAL ADVANCEMENT AND RETROGRADATION (GREEN WAVE EFFECT) OF NATURAL VEGETATION* (Goddard Space Flight Center, Greenbelt, MD, USA).

24. Asner GP, et al. (2016) Progressive forest canopy water loss during the 20122015 California drought. *Proceedings of the National Academy of Sciences* 113(2):E249–E255.

25. Young DJN, et al. (2017) Long-term climate and competition explain forest mortality patterns under extreme drought. *Ecology Letters* 20(1):78–86.

26. Wood EM, Pidgeon AM, Radeloff VC, Keuler NS (2012) Image texture as a remotely sensed measure of vegetation structure. *Remote Sensing of Environment* 121:516–526.

27. Huang Q, Swatantran A, Dubayah R, Goetz SJ (2014) The Influence of Vegetation Height Heterogeneity on Forest and Woodland Bird Species Richness across the United States. *PLoS ONE* 9(8):e103236.

28. Stein A, Gerstner K, Kreft H (2014) Environmental heterogeneity as a universal driver of species richness across taxa, biomes and spatial scales. *Ecology Letters* 17(7):866–880.

29. Tuanmu M-N, Jetz W (2015) A global, remote sensing-based characterization of terrestrial habitat heterogeneity for biodiversity and ecosystem modelling: Global habitat heterogeneity. *Global Ecology and Biogeography* 24(11):1329–1339.

30. Graham LJ, Spake R, Gillings S, Watts K, Eigenbrod F (2019) Incorporating fine-scale environmental

heterogeneity into broad-extent models. *Methods in Ecology and Evolution* 10(6):767–778.

31. Kéfi S, et al. (2014) Early Warning Signals of Ecological Transitions: Methods for Spatial Patterns. *PLoS ONE* 9(3):e92097.

32. Haralick RM, Shanmugam K, Dinstein I (1973) Textural Features for Image Classification. *IEEE Transactions on Systems, Man, and Cybernetics* SMC-3(6):610–621.

33. Gao B-c (1996) NDWIA normalized difference water index for remote sensing of vegetation liquid water from space. *Remote Sensing of Environment* 58(3):257–266.

34. Huesca M, García M, Roth KL, Casas A, Ustin SL (2016) Canopy structural attributes derived from AVIRIS imaging spectroscopy data in a mixed broadleaf/conifer forest. *Remote Sensing of Environment* 182:208–226.

35. García ML, Caselles V (1991) Mapping burns and natural reforestation using thematic Mapper data. *Geocarto International* 6(1):31–37.

36. USGS (2017) Landsat 8 Surface Reflectance Code (LASRC) Product Guide. 40.

37. USGS (2017) Landsat 4-7 Surface Reflectance (LEDAPS) Product Guide. 41.

38. McCune B, Keon D (2002) Equations for potential annual direct incident radiation and heat load. *Journal of Vegetation Science* 13(4):603–606.

39. McCune B (2007) Improved estimates of incident radiation and heat load using non- parametric regression against topographic variables. *Journal of Vegetation Science* 18(5):751–754.